Appl Phys B (2011) 105:149–162
DOI 10.1007/s00340-011-4766-y

Applied Physics B
Lasers and Optics

Investigation of the nonlinear optical properties of metamaterials by second harmonic generation

M. Gentile · M. Hentschel · R. Taubert · H. Guo · H. Giessen · M. Fiebig

Received: 7 June 2011 / Revised version: 26 August 2011 / Published online: 28 September 2011
© Springer-Verlag 2011

Abstract Nonlinear optical spectroscopy is applied to two types of metamaterials: (i) variations of split-ring resonators fabricated as periodic two-dimensional arrays of gold on SiO_2, and (ii) gratings of periodically spaced straight wires of gold on multiferroic hexagonal single crystals from the $R\mathrm{MnO_3}$ family. Optical second harmonic generation (SHG) on samples of type (i) is used to characterize the nonlinear response of metamaterials in dependence of the photon energy and the size, shape, and symmetry of the nanoscopic building blocks constituting the metamaterials. We find a complex dependence of the SHG spectra on the design parameters that requires an in-depth theoretical analysis. SHG is applied to samples of type (ii) to enhance the nonlinear optical performance of functional materials by writing a metamaterial acting as optical catalyst on top. We observe an enhancement of the SHG signal induced by the ferroelectric order of the $R\mathrm{MnO_3}$ crystals, yet with pronounced variations between samples. Measurements of both types, (i) and (ii), show that a comprehensive understanding of the nonlinear optical properties of metamaterials requires one to go beyond a macroscopic symmetry treatment. In fact, structural inhomogeneities on the level of the nanoscopic building blocks have a major impact.

M. Gentile · M. Fiebig (✉)
Helmholtz-Institut für Strahlen- und Kernphysik, Universität Bonn, Nussallee 14-16, 53115 Bonn, Germany
e-mail: fiebig@hiskp.uni-bonn.de

M. Gentile
e-mail: gentile@hiskp.uni-bonn.de

M. Hentschel · R. Taubert · H. Guo · H. Giessen
4. Physikalisches Institut und Research Center SCoPE, Universität Stuttgart, Pfaffenwaldring 57, 70550 Stuttgart, Germany

1 Introduction

From initial theoretical investigations [1] to conceptual breakthrough [2] and realization [3], the concept of metamaterials has revolutionized the field of optics. Metamaterials are artificial materials with designed electromagnetic functionality. They represent a periodic arrangement of building blocks with a size much smaller than the wavelength of their electromagnetic resonances [4–7]. The working range extends from microwaves and millimeter-sized designs toward the optical range with structures in the order of 100 nm, typically fabricated with gold on glass [8]. Not only the dielectric function of the metal and of the surrounding environment play a major role for the optical properties, but also the size and shape of the nano-scaled building blocks [9, 10]. A variety of shapes has been employed: From simple spheres and ellipsoids to wires [11, 12], split-ring resonator (SRR) designs [2, 13], meshes [14, 15], meanders [16, 17], or swiss-rolls [2, 4].

Thus, in addition to exploiting the broad variety of materials provided by nature, researchers can now *engineer* new optical properties by design. A wealth of features not found in nature have been proposed. For instance, a negative magnetic permeability μ [2, 11–13, 18] along with a negative electric permittivity ε [19] lead to metamaterials in which the refractive index becomes negative [5, 7]. As predicted by Veselago [1], strikingly unusual phenomena occur in these materials. For example, the electric and magnetic field vectors (**E**, **H**) and the wave vector **k** can form a so-called left-handed system in which the wave fronts travel in a direction opposite to that of the energy transport. In terms of application, these astonishing properties could lead to novel devices such as perfect lenses, beating the Abbe diffraction limit [20–22], and optical cloaks, rendering objects invisible [23–26].

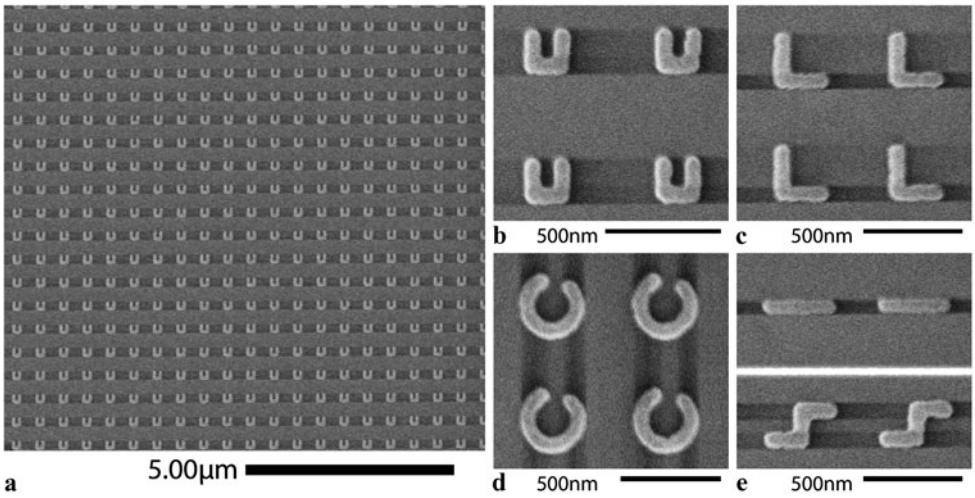

Fig. 1 SEM micrographs of gold structures written on a glass substrate. The image *on the left* demonstrates the uniformity of our structures across large distances. The shadows between the nanostructures are caused by the screening of secondary electrons by the metal

Most of the recent publications on metamaterials, including this work, are based on two predictions [2]. First, SRRs are proposed as functional unit cells as shown in Fig. 1a. Initially, each SRR was interpreted as a coil with a single winding that guides plasmonic oscillations, and, additionally, as a capacitance associated with the inserted slit. Thus, one obtains the nanoscopic equivalent of an *LC* resonance circuit. Nowadays, the widely accepted interpretation of the resonances consists of static plasmonic waves [27]. This leads to qualitatively new and unprecedented behavior and attracted substantial effort from both experiment [13, 28–33] and theory [34–36]. Second, enhanced nonlinear optical properties were predicted to arise from gold nanostructures, e.g. the emergence of a giant *nonlinear* optical response through local-field enhancement [35, 37, 38].

Nonlinear optics, in particular the lowest-order process second harmonic generation (SHG), offers a variety of advantages in comparison to its linear counterpart. It constitutes an improved characterization tool [39–43]: Nonlinear optical processes reveal novel information about materials, see e.g. the nonlinear Kerr effect [43]. Based on the involvement of more than a single light field, additional experimental degrees of freedom are available. New states become accessible by multiphoton transitions. Through its higher selectivity (in terms of photon energy, wavevector, and light polarization) nonlinear optical spectroscopy is a key for identifying the microscopic processes at play in a material. Also, the high intensity of the light fields involved in nonlinear optical excitations can lead to a modification of the optical properties of the material and thus results in new functionalities.

Hence, nonlinear optics is a powerful tool for the characterization as well as for the functional use of materials. Yet its application to the investigation of metamaterials remained quiescent for some time. No experimental reports or suggestions for a consistent microscopic theory of the nonlinear optical properties of metamaterials was reported before the work of Klein et al. [44, 45]. In this pioneering work, the nonlinear response of SRRs was investigated and a microscopic description based on a Lorentz force model was proposed. Since measurements were carried out at a fixed excitation frequency and limited to a single type of structure, the access to the microscopic mechanisms determining the nonlinear optical response of metamaterials remained limited. Aside from spectroscopy and shape variation, the interaction between the individual "meta-atoms" [46, 47] was not considered. Thus, the debate on the nonlinear optical performance of metamaterials remains a widely open field of research [48–54].

In this work, SHG spectroscopy is employed for investigating the nonlinear optical response of metamaterials in two complementary ways. On the one hand, the nonlinear optical performance is *characterized* by performing SHG spectroscopy on a variety of metamaterials differing in size, shape, and symmetry. On the other hand, the nonlinear optical performance is *applied* to manipulate the nonlinear optical response of the host system (substrate) onto which the metamaterials are deposited. Insights into the potential of metamaterials are gained in both cases, but a clear need to continue the experiments for obtaining a comprehensive picture of metamaterials as a nonlinear medium is also recognized.

In the following, we provide a brief introduction to the fundamentals of linear and nonlinear optics on metals at the nanometer scale; see Sect. 2. A description of the samples is given in Sect. 3, while the experimental methods are detailed in Sect. 4. The experimental results on the *characterization* and *application* of these metamaterials are discussed in Sect. 5.1 and Sect. 5.2, respectively.

2 Nanoscale optical principles

2.1 Linear optics

All electromagnetic phenomena in matter are governed by Maxwell's equations:

$$\nabla \cdot \mathbf{D} = \rho, \qquad \nabla \cdot \mathbf{B} = 0, \qquad \nabla \times \mathbf{E} = -\frac{\partial \mathbf{B}}{\partial t}, \qquad \nabla \times \mathbf{H} = \frac{\partial \mathbf{D}}{\partial t} + \mathbf{j}. \tag{1}$$

Here, $\mathbf{E}$ is the electric field, $\mathbf{H}$ is the magnetic field, $\mathbf{D} = \varepsilon_0 \mathbf{E} + \mathbf{P} = \varepsilon_0 \varepsilon \mathbf{E}$ is the electric displacement, and $\mathbf{B} = \mu_0(\mathbf{H} + \mathbf{M}) = \mu_0 \mu \mathbf{H}$ is the magnetic induction. The permittivity of the vacuum and the material are denoted as ε_0 and ε, respectively, and $\mathbf{P}$ is the electric polarization. The permeability of the vacuum and the material are denoted as μ_0 and μ, respectively, and $\mathbf{M}$ is the magnetization. The electric charge density ρ and the electric current density $\mathbf{j}$ are related by the charge conservation law $\nabla \cdot \mathbf{j} + \frac{\partial \rho}{\partial t} = 0$.

Introducing the vacuum speed of light, $c_0 = 1/\sqrt{\varepsilon_0 \mu_0}$, one can derive the wave equation for linear optics:

$$\Delta \mathbf{E} + \frac{\varepsilon}{c_0^2} \frac{\partial^2}{\partial t^2} \mathbf{E} = 0. \tag{2}$$

2.2 Perturbative nonlinear optics

Since the development of the laser [55], very high electric field strengths inaccessible to any other light source have become available. For pulsed lasers, values as high as $E = 1 \times 10^{20}\ \mathrm{V\,m^{-1}}$ are possible (interatomic electric fields are of the order of $1 \times 10^{8}\ \mathrm{V\,m^{-1}}$). At these intensities, nonlinear terms in the electric polarization and magnetization have to be considered, and (2) evolves into the nonlinear optical wave equation:

$$\Delta \mathbf{E} + \frac{\varepsilon}{c_0^2} \frac{\partial^2}{\partial t^2} \mathbf{E} = \mathbf{S}, \tag{3}$$

where $\mathbf{S}$ is the source term driving the nonlinear optical wave. For instance, when light with the frequency ω and the electric field $\mathbf{E}(\omega)$ is incident on a material, harmonic generation can lead to an electromagnetic polarization at frequency 2ω. This acts as source term $\mathbf{S}(2\omega)$ for an SHG light wave [39]. It is possible to express the source term by the multipole expansion [41],

$$\mathbf{S} = \mu_0 \frac{\partial^2 \mathbf{P}_{\mathrm{NL}}}{\partial t^2} + \mu_0 \left(\nabla \times \frac{\partial \mathbf{M}_{\mathrm{NL}}}{\partial t} \right) - \mu_0 \left(\nabla \frac{\partial^2 \hat{\mathbf{Q}}_{\mathrm{NL}}}{\partial t^2} \right), \tag{4}$$

where $\mathbf{P}_{\mathrm{NL}}$, $\mathbf{M}_{\mathrm{NL}}$, and $\hat{\mathbf{Q}}_{\mathrm{NL}}$ are the electric dipole (ED), magnetic dipole (MD), and electric quadrupole (EQ) moments, respectively.

Taking terms of the order 0 and 1 in the expansion of the electromagnetic field into account, the following contributions, associated to the ED, MD, and EQ, are obtained [56–58]:
zeroth order:

$$\mathbf{P}_{i,\mathrm{NL}} = \chi_{ijk}^{(2),\mathrm{ED}} : \mathbf{E}_j \mathbf{E}_k, \tag{5}$$

first order:

$$\mathbf{P}_{i,\mathrm{NL}} = \chi_{ijk}^{(2),\mathrm{MD}} : \mathbf{E}_j \mathbf{B}_k + \chi_{ijkl}^{(2),\mathrm{EQ}} : \mathbf{E}_j \nabla_k \mathbf{E}_l, \tag{6}$$

$$\mathbf{M}_{i,\mathrm{NL}} = \chi_{ijk}^{(2),\mathrm{MD}} : \mathbf{E}_j \mathbf{E}_k, \tag{7}$$

$$\hat{\mathbf{Q}}_{ij,\mathrm{NL}} = \chi_{ijkl}^{(2),\mathrm{EQ}} : \mathbf{E}_k \mathbf{E}_l. \tag{8}$$

Equation (6) involves MD and EQ effects at the fundamental frequency ω while in (7) and (8) the magnetization and quadrupolarization at 2ω is considered. Additionally, emission from the quadrupolarization involves a gradient of the source with respect to the direction of propagation $\nabla_i \hat{\mathbf{Q}}_{ij}$.

Each term can contribute to the SHG process. However, the magnetic dipole and electric quadrupole contributions in crystalline solids are smaller than the electric dipole by a factor $\lambda/a \sim 10^3$, where λ is the radiation wavelength and a is the lattice constant of the crystal. Therefore, they can often be neglected which is termed as electric-dipole approximation.

The tensor χ denotes the nonlinear susceptibility. Following the Neumann principle, the symmetry of the sample determines the set of tensor components $\chi_{ijk} \neq 0$ (with $i, j, k \in \{x, y, z\}$), see Sect. 3.2 and Sect. 3.4. Hence, due to symmetry reasons, an electromagnetic wave incident on a centrosymmetric structure or on an isotropic continuous metal surface at normal incidence (or oblique to this surface in s-polarization) cannot create an ED-SHG wave according to (5) [59, 60]. Such a sensitivity to structure and symmetry makes SHG a key technique for investigating the effects of shape, structure, and symmetry. The intensity of the nonlinear signal is spectrally sharp at 2ω and proportional to the square of the source term:

$$I \propto |\mathbf{S}|^2. \tag{9}$$

These criteria are unique signatures distinguishing SHG signals from other optical processes such as photoluminescence.

2.3 Optics of metallic nanoparticles

To describe the interaction of the electromagnetic light field with the sub-wavelength structures of a metamaterial, we consider qualitatively the plasmon scattering effect on the linear spectra.

The interaction of metals with electromagnetic radiation is largely dictated by the free conduction electrons in the metal. According to the Drude model, it is possible to describe a metal by a free electron gas moving between heavier, stationary crystal ions [61]. Driven with an harmonic electric field **E** of frequency ω, the electrons with mass m_e, charge $-e$ and density n_e build up a polarization from which one can derive a relative permittivity ε_D to describe the metal:

$$\varepsilon_\mathrm{D}(\omega) = 1 - \frac{\omega_\mathrm{pl}^2}{\omega(\omega + i\gamma_c)}. \tag{10}$$

Here, $\omega_\mathrm{pl} = \sqrt{(n_e e^2)/(\varepsilon_0 m_e)}$ is the so-called bulk plasma frequency of the Drude metal and γ_c is the collision rate, representing Ohmic damping. For gold, the model is in excellent agreement with the experimental data by Johnson et al. for photon energies up to 2.3 eV [62]. For higher photon energies, deviations from experimental data are explained by interband transitions, giving the metal its color.

Defining the complex refractive index $n = \sqrt{\varepsilon_\mathrm{D}} = n_r + i\kappa$, the penetration depth of an electromagnetic radiation incident on a metal surface is given by $\delta = c_0/(\omega\kappa)$. Typical penetration depths are in the order of the thickness of the structures used in this work so that the penetration of the transverse electric field into the metamaterial is considerable.

Considering metallic nanoparticles (the "unit cell" building blocks of the metamaterial) rather than a plain film, one has to account for finite volumes and highly curved surfaces. An analytical description of the optical properties of spherical particles is provided within the framework of Mie theory [63]. With particles much smaller than the fundamental wavelength, the electric field of light shifts the conduction electrons with respect to the ionic background. This creates a depolarization field driving the electrons into a collective oscillation. Its eigenmodes are called particle plasmons. The eigenfrequency of a particle plasmon is given by

$$\Omega_\mathrm{PP} = \sqrt{L_i}\,\omega_\mathrm{pl}. \tag{11}$$

L_i is called the depolarization factor for which, generally, $\sum_i L_i = 1$, where $i \in \{x, y, z\}$ corresponds to the principal axes of an ellipsoidal particle. The longer the axis, the smaller the depolarization factor. This qualitative dependence is used to tune the plasmon frequency for gold nanowires, as those used in Sect. 3.3. More complex and arbitrary shapes as those described in Sect. 3.1 require elaborate numerical methods [64] to access the modes and field distributions.

A particle plasmon forms an oscillating electric–dipole moment that radiates with an emission spectrum whose width is dominated by radiative energy losses. Also, an incident electromagnetic light field can couple to the dipole and it is possible to describe the system as a harmonic Lorentz oscillator following the equation of motion:

$$\ddot{x} + 2\gamma\dot{x} + \Omega_0^2 x = \frac{q}{m}E. \tag{12}$$

E is the driving electric field, x the displacement, q the effective charge, m the effective mass, $\Omega = \sqrt{\Omega_0^2 - \gamma^2}$ the damped eigenfrequency, $\gamma = 1/T_2 = 1/(2\tau)$ the half-width/half-maximum value, T_2 the dephasing time, and τ the plasmon decay time in the order of 5 fs [65, 66]. Such a short decay time reflects the fact that excitations of collective electron oscillations is easily excited with light. Unfortunately, this also means that the dephasing time T_2 is very short for particle plasmons due to the strong radiative loss. This limits the time for coherent light-matter interaction as well as the local field enhancement factor, which is proportional to T_2 [65, 67].

3 Samples

In this section, we describe the two systems employed for the previously introduced experiments on the characterization and application of metamaterials: gold nanostructures on glass and gold nanowires on $R\mathrm{MnO_3}$, respectively.

3.1 Gold on glass: fabrication

As the basic structure of this investigation we chose the most commonly studied metamaterial building block: ⊔-shaped SRRs. The structure is easily scalable, and basic design variations in symmetry and shape complexity allow us to investigate the effects these parameters have on the SHG performance. The samples used in this work were fabricated in the group of H. Giessen at the University of Stuttgart. The sub-wavelength building blocks consist of a nanostructured gold film on a Heraeus Suprasil 1 quartz glass substrate. The structures are defined by electron-beam lithography in a spin-coated poly(methyl methacrylate) (PMMA) positive photoresist followed by thermal evaporation of a 3 nm chromium adhesion layer and a gold film of 30 nm followed by a lift-off procedure. The lateral size of each array is about $200 \times 200\ \mu\mathrm{m}^2$ with a field-to-field distance in the order of 200 µm.

Seven design variations as depicted in Fig. 2 were measured. They allow us to investigate the effects of a variation of size, shape complexity and symmetry in comparison to the basic ⊔ structure:

(i) The reference building block consists of a classical ⊔-shaped SRR of approximately 240 nm base length with an arm-to-base length ratio close to one. A linear resonance in the range 0.65–1.45 eV with a width of 0.20–0.35 eV is observed.

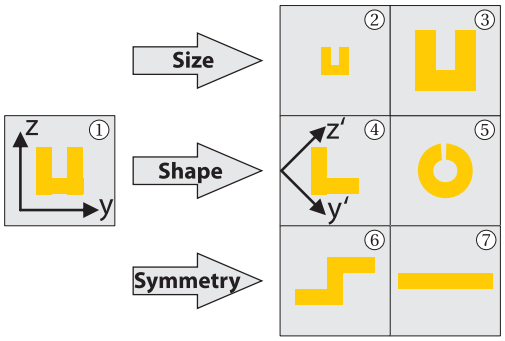

Fig. 2 Schematic geometry of the building blocks for the metamaterials fabricated as two-dimensional periodic arrays of gold on glass. The geometries were selected for investigating the effects of size, shape, and symmetry on the nonlinear optical performance. The Cartesian coordinate system is oriented according to [59]. The L-shaped structures require a 45° rotation of their coordinate system to match the nomenclature and symmetry operations used for the description of the other structures

(ii) The effect of size scaling was investigated with the second and third designs. The former increases both the base and arm lengths to achieve a linear resonance at lower energies, while the latter reduces them to obtain a linear resonance at higher energy. Note that in contrast to the approach by Klein et al., who substitute spectroscopy by geometric scaling in their experiments, we directly compare the effects of scaling and spectroscopy in the present approach.

(iii) All further shape variations were adapted to ensure a linear resonance matched to the first design. Designs number 4 and 5 give insight into the effect of complexity. We retain the basic shape of an SRR but we reduce the number of corners in the design. Corners are associated with local field peaks and may favor higher-order nonlinear contributions, e.g. according to (4). The elementary unit in configuration 4 presents a single arm and has consequently one pair of corners less in an L-shaped geometry [68–71]. The 5th design avoids corners even further with its C-shaped geometry.

(iv) Finally, centrosymmetric structures were produced in the form of the last two layouts. For these structures any SHG emission is forbidden in the ED approximation so that higher-multipole or local contributions according to Sect. 2.3 become observable. Pattern number 6 differs from the original design only in that one arm is flipped with respect to the base. Thus, we are changing only the symmetry while retaining the shape complexity. The last design, number 7, represents a simple cut-wire geometry, i.e. a ⊔ design after unfolding the arms.

Finally, a reference sample consisting of a bare gold film of same thickness as used for the metamaterials which covered half the area of the substrate was produced. Its use in the evaluation for the damage threshold for laser irradiation is discussed in Sect. 4.3.

Electron micrographs of the fabricated structures are obtained by field emission scanning electron microscopy (SEM), using a Hitachi S-4800 electron microscope. Figure 1 shows normal-incidence images of some of the structures investigated in this work. The SEM images demonstrate the good uniformity of the fabricated structures across large distances. The structures are mechanically very stable and withhold aggressive manufacturing steps such as pressured air flow and ultrasound bath of acetone.

Table 1 Non-zero ED-type SHG tensor components and polarization configurations for the non-centrosymmetric point group $mm2$. Polarizations are denoted by p (parallel to the plane of incidence), s (parallel to the sample surface) and d (at 45° between the p and s polarizations)

Polarization configuration		SHG susceptibility
Ingoing	Outgoing	
s	s	χ_{zzz}
p	s	χ_{zyy}
d	p	$\chi_{yyz} = \chi_{yzy}$

3.2 Gold on glass: SHG tensor components

Here and in Sect. 3.4, we consider an effective SHG susceptibility describing the global symmetry of a periodic arrangement of *ideal* gold nanostructures. Herewith, we neglect local deviations from the model design in the individual structures. It is one purpose of this work to verify the validity of this approach, see Sect. 5.1.

The designs 1 to 5 in Fig. 2 all share the same symmetry. The coordinate system shown in each sketch is oriented according to [59] with z representing the axis with the highest symmetry.

In the case of the non-centrosymmetric structures, operations 1, $\overline{2}_x$, $\overline{2}_y$ and 2_z leave the structures invariant. This corresponds to an orthorhombic symmetry according to the point group $mm2$. In the ED approximation, see (5), the only non-zero tensor components for a sample with $mm2$ symmetry are: $\chi_{xxz} = \chi_{xzx}, \chi_{zxx}, \chi_{zzz}, \chi_{yyz} = \chi_{yzy}$ and χ_{zyy}. However, at normal incidence, with a beam propagating along the x-axis, all the susceptibilities with one or more indices x are inaccessible because of the transverse polarization of the light. This leaves only three independent tensor components, namely χ_{zzz}, $\chi_{yyz} = \chi_{yzy}$, and χ_{zyy}. The experimental configurations for accessing these components are listed in Table 1. We stress that in the χ_{yzy} configuration, the forbidden χ_{yyy} and χ_{yzz} contributions are also analyzed simultaneously. For the MD as well as for the EQ approximation, no tensor components are accessible for light at normal incidence ($\mathbf{k} \parallel \mathbf{x}$) according to [59].

For centrosymmetric structures, operations 1, $\overline{1}$, 2_x, and $\overline{2}_x$, leave design 6 invariant, while design 7 has a higher symmetry that operations 1, $\overline{1}$, 2_x, 2_y, 2_z, $\overline{2}_x$, $\overline{2}_y$ and $\overline{2}_z$, leave invariant. This corresponds to monoclinic and orthorhombic structures with the point symmetry $2/m$ and mmm, respectively. As mentioned in Sect. 2.2, the inversion symmetry suppresses SHG in the leading ED order. As for the point symmetry $mm2$, MD and EQ contributions to SHG are also forbidden at normal incidence, so that no SHG emission from these structures is expected.

3.3 Gold on hexagonal $R\mathrm{MnO_3}$: fabrication

The basic manufacturing steps were similar to those described in Sect. 3.1. However, simple gold nanowires replaced the ⊔ structures, and the glass substrate was replaced by a c-cut hexagonal crystal from the multiferroic $R\mathrm{MnO_3}$ family, see Sect. 3.4. The wires can enhance the SHG yield of the crystals by tailoring the electromagnetic light field within the sample, yet without being a source of SHG themselves because of their centrosymmetric shape. They can thus act as an optical field enhancement device.

The described method is general enough to be applied to *any* kind of material. However, we need a model compound allowing us to study both the *mechanism* and the *functionality* of the SHG enhancement. This leads to the hexagonal manganites as a model system. The isomorphous $R\mathrm{MnO_3}$ crystals (R = Sc, Y, In, Dy-Lu) belong to the family of multiferroics, i.e. compounds displaying simultaneous long-range electric and magnetic order [72]. SHG is particularly useful for the simultaneous investigation of the two forms of ordering and thus their interaction. Both the ferroelectric (FEL) and the antiferromagnetic (AFM) order of the hexagonal $R\mathrm{MnO_3}$ system were extensively investigated by SHG whose spectral, polarization, spatial, and temperature dependencies are very well known [73, 74]. In our experiment we employed both the FEL and the AFM contribution to the SHG signal. The basic mechanism of the SHG enhancement was verified under ambient conditions in the broad spectral range accessible with FEL SHG. The functionality of the SHG enhancement was investigated by monitoring the response of the AFM domains to the metamaterial applied to the $R\mathrm{MnO_3}$ samples. This experiment was carried out at cryogenic conditions, employing the AFM SHG signal.

The gold wires were fabricated on $\mathrm{YbMnO_3}$ and $\mathrm{HoMnO_3}$ crystals grown either by the flux or the floating-zone technique. They form gratings with an extension of 200 × 200 $\mu\mathrm{m}^2$. The linear resonance of the wires is placed in the range from 0.82 eV up to 1.46 eV. Note that at 1.20 eV the maximum yield of the AFM SHG signal is obtained. As described in Sect. 2.3, the electric field of a light wave polarized perpendicular to the wires drives a collective electron oscillation leading to an electric field enhancement localized at the edge of the wires. The quadratic dependence expressed by (9) should then lead to dramatic enhancement of SHG efficiency within the crystal, depending on the wire orientation with respect to the crystal axes. Thus, after optical polishing each $R\mathrm{MnO_3}$ substrate was oriented using Laue diffraction. Thereafter, wires were fabricated either parallel or perpendicular to the crystallographic x-axis. Here, a Cartesian coordinate system is used which is related to the hexagonal unit-cell axes by $z = c$ and $x = a$. Using such a design, one can probe the effect of local field enhancement in the non-centrosymmetric $R\mathrm{MnO_3}$ while suppressing SHG contributions from the centrosymmetric wires.

3.4 Hexagonal $R\mathrm{MnO_3}$: SHG tensor components

$R\mathrm{MnO_3}$ crystals possess a hexagonal unit cell and a fivefold coordination of the central Mn^{3+} ion [73]. Above the Curie temperature $T_C \approx 600$–1000 K, the compound is paraelectric and paramagnetic, possessing the space symmetry $P6_3/mmc$ [59]. At T_C, a FEL distortion leads to a spontaneous polarization P along the hexagonal axis. P is the ferroelectric order parameter which transforms like an i-type scalar [59, 75]. The ferroelectric ordering breaks the inversion symmetry and reduces the symmetry to $P6_3cm$. At the Néel temperature $T_N \approx 70$–130 K, AFM ordering of the Mn^{3+} spins breaks the time-reversal symmetry of the crystal. The AFM order parameter of the triangular spin lattice is l. It transforms like the component of a third-rank axial c tensor [59, 75] and reduces the symmetry of the simultaneously FEL and AFM lattice to $P\underline{6}_3/c\underline{m}$ or $P\underline{6}_3/\underline{c}m$.

The SHG contributions for hexagonal $R\mathrm{MnO_3}$ are listed in Table 2. AFM contributions to SHG involve x-polarized and y-polarized light only, while for all ferroelectric contributions at least one z-polarized light wave contributes. Hence, the AFM order is best observed with light incident along the z axis where ferroelectric SHG contributions cannot be excited. In turn, an investigation of the FEL order is only possible with light *not* incident along the z axis. Here, mixing with AFM contributions to SHG is avoided by a suitable choice of polarizations or by performing the experiment at $T > T_N$ where the AFM SHG contribution is zero.

Table 2 Tensor components for SHG in hexagonal $R\mathrm{MnO_3}$ according to (5) and Ref. [59] using Cartesian coordinates

Space symmetry	SHG tensor components
	Ferroelectric
$P6_3cm$	$\chi_{zzz}, \chi_{zxx} = \chi_{zyy}, \chi_{xxz} = \chi_{yyz}$
	Antiferromagnetic
$P\underline{6}_3\underline{c}m$	$\chi_{xxx} = -\chi_{xyy} = -\chi_{yxy} = -\chi_{yyx}$
$P\underline{6}_3c\underline{m}$	$\chi_{yyy} = -\chi_{yxx} = -\chi_{xyx} = -\chi_{xxy}$

An SHG signal of FEL origin is observable in the broad 1.2–3.0 eV range. Adversely, the usable range for AFM SHG contributions across the $R\mathrm{MnO_3}$ family is restricted to the much narrower 2.3–2.8 eV range. A detailed discussion of SHG spectroscopy on the $R\mathrm{MnO_3}$ system is found in [72] and [73].

4 Experiment: methods

4.1 Linear optical characterization

To obtain reasonable structural parameters for design and fabrication of the samples, linear spectra were calculated using a finite integration technique (commercial software package CST Microwave Studio, Darmstadt, Germany). In the calculations the structures were placed on a quartz ($n = 1.46$) or an $R\mathrm{MnO_3}$ substrate and surrounded by air. The dielectric materials were assumed dispersion free. For gold, a Drude model was used, see Sect. 2.3. The linear spectra are experimentally determined using a Fourier transform infrared spectrometer (Bruker Vertex 80) with an attached microscope (Bruker Hyperion, 15x Cassegrain objective, NA 0.4). For the measurements we used linearly polarized light at normal incidence. Detection was performed with a liquid-nitrogen-cooled mercury-cadmium-telluride (MCT) detector and a silicon diode.

4.2 Setup for SHG spectroscopy

In the present SHG spectroscopy experiment, frequency-tunable laser pulses of 120 fs were generated at 1 kHz by an optical parametric amplifier (OPA) pumped by a Ti:Sapphire regenerative amplifier system. Depending on the photon energy, the laser pulses emitted by the OPA had a fluence of 30 to 300 $\mathrm{mJ\,cm^{-2}}$. However, the fluence was reduced to 2.3 $\mathrm{mJ\,cm^{-2}}$ across the whole spectral range to protect the samples from destruction, see Sect. 4.3. Hence, light pulses of 0.7 µJ with a photon energy of 0.76–1.57 eV were focused on a spot with a diameter of about 200 µm.

A Glan–Taylor prism paired with a half-wave plate and optical long-pass filters were used to set the polarization of the incoming light and block higher harmonics generated in the optical components. Short-pass filters and a second Glan–Taylor prism were used to separate the fundamental and the SHG light behind the sample and analyze the polarization of the SHG signal. A lens was used to project the signal light through an imaging spectrograph onto a liquid-nitrogen-cooled digital camera. There, the signal was integrated in the spectroscopic experiments or spatially resolved for a precise alignment of the laser beam with respect to the metamaterial array. Considering the low excitation density, the low conversion efficiency of the nonlinear optical process and the low thickness of the material contributing to SHG, the very low dark current of the camera (four electrons per pixel and hour) and its high average quantum efficiency (∼50%) are a key for obtaining a detectable SHG signal.

In the SHG spectroscopy of gold metamaterials on a glass substrate, light is incident on the sample at normal incidence in transmission geometry. The SHG enhancement involving gold on $R\mathrm{MnO_3}$ substrates was measured in reflection geometry. The SHG signals of FEL origin was obtained with light incident at 45° to the sample surface to access the z component, which is present in all the tensor components contributing to FEL SHG, see Sect. 3.4. The SHG signals of AFM origin was measured at near-normal incidence (angle ≤2°) to detect the AFM SHG and suppress any FEL SHG. Because of their cryogenic Néel temperature, the $R\mathrm{MnO_3}$ samples were mounted in an optical cryostat operated with liquid helium.

The linewidth of the fundamental beam was about 3 meV which was therefore the smallest reasonable increment in the spectroscopy measurements. A finer spectral resolution would be obtained with a Nd:YAG laser emitting nanosecond laser pulses. However, no detectable SHG is obtained with such a laser system.

Nonlinear spectroscopy with femtosecond laser pulses depends critically on the normalization procedure applied to the data. There are two ways to perform intensity normalization. Most commonly, the spectral response function $f(\omega)$ including the transmission of the optical filters and of the monochromator grating and the quantum efficiency of the camera is calculated by referring to the respective lookup tables. When measuring the pulse energy of the fundamental light with a flat-response Joule meter one can normalize the SHG data to the intensity of the incident light: $I_{2\omega}^{\mathrm{norm.}} = I_{2\omega}^{\mathrm{meas.}}/f(\omega) \cdot I_{\omega}^{2}$, with $I_{2\omega}^{\mathrm{norm.}}$ as normalized SHG intensity, $I_{2\omega}^{\mathrm{meas.}}$ as measured SHG intensity, and I_{ω} as intensity of the fundamental wave. However, this approach does not account for the spectral or temporal variations of the pulse length or the beam profile. Therefore, in a refined normalization procedure, the sample is replaced with a reference SHG source with spectrally flat SHG response such as the surface of a silver mirror in our case. This leads to a normalized SHG intensity according to $I_{2\omega}^{\mathrm{norm.}} = I_{2\omega}^{\mathrm{meas.}}/I_{2\omega}^{\mathrm{ref.}}$, with $I_{2\omega}^{\mathrm{ref.}}$ the reference SHG intensity. Note that, with this approach, the spectral response function of the setup, $f(\omega)$, is automatically included in the normalization. Since the setup responds differently to s- and p-polarized light, both reference configurations have to be measured. Figure 3 clearly demonstrates that application of the refined procedure is indispensable for proper normalization as it reveals a pronounced discrepancy between the results of the two normalizing procedures.

During the acquisition of the SHG spectra, we observed spectral shifts in the beam position by ca. 30 µm, mainly due to moving components in the OPA. There are three ways to overcome this: Manual adjustment, automated adjustment,

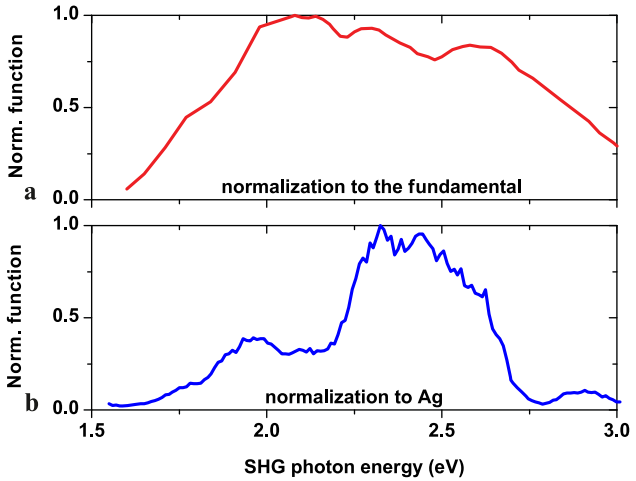

Fig. 3 Normalization functions: (**a**) normalization to the spectral transmission of the optical setup and the intensity of the incident fundamental light ($f(\omega) \cdot I_{\omega}^{2}$, see Sect. 4.2) or (**b**) to the SHG signal obtained on a reference sample with a spectrally broad and flat SHG response, here a silver mirror ($I_{2\omega}^{\mathrm{ref}}$). The comparison reveals that only the latter normalization procedure is appropriate

or an increase of the area covered by the metamaterial. On the one hand, manual adjustment means time-consuming piece-wise spectral acquisition. Due to chromatic aberration, the same holds true for passive $4f$-imaging systems. On the other hand, automation based on a pyrometric quadrant detector and a coupled motorized motor leads to an increase in complexity of the setup. Thus, we decided to work with particularly large $200 \times 200\ \mu\mathrm{m}^2$ metamaterial fields, as described in Sect. 3.1. This, together with an improved adjustment procedure of the laser system, leads to a stable overlap of the laser beam and the area covered by the metamaterial.

4.3 Sample damage

Illumination of the samples with intense femtosecond laser radiation can lead to alterations or, in the worst case, to the complete destruction of the metamaterials, see Fig. 4. Therefore, we had to find a procedure for maximizing the SHG signal without destroying our samples. On the one hand, use of a regenerative amplifier laser system is essential to produce measurable SHG signals, whereas with a non-amplified system with a repetition rate in the Megahertz regime this is not possible without excessively long exposure time. On the other hand, the high pulse intensities obtained at a repetition rate of 1 kHz deposits a considerable amount of energy into the sample with the potential to cause damage.

Therefore, it is essential to estimate the damage threshold of the samples. For this purpose we used the reference sample with the half-coated continuous gold film mentioned in Sect. 3.1. The metamaterial arrays do not consist of a

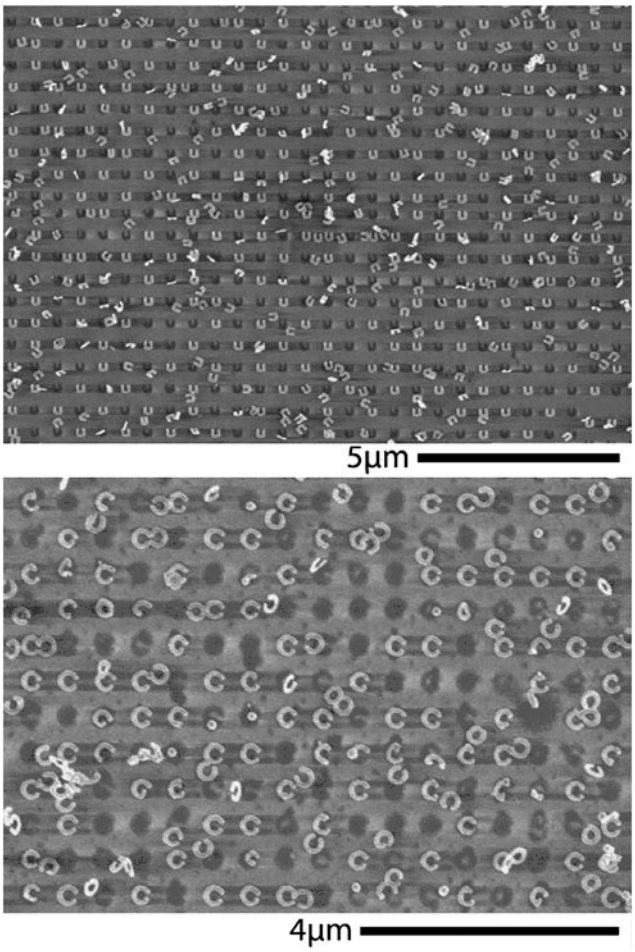

Fig. 4 SEM micrographs of gold metamaterials on a glass substrate. Intense laser radiation can destroy the periodic arrangement of the building blocks up to partial detachment and relocation on the substrate without yet melting the gold. The present images were obtained after illumination with amplified laser pulses at 120 fs and 0.7–1.6 eV with a power of 2.3 mJ cm^{-2}

closed layer of gold, but of nanostructures with numerous gold-substrate transitions. Therefore, the reference sample was positioned such that the focused beam hits the edge of the coated area. This was based on the assumption that the threshold for damage at the edges is lower than in the center of a continuous layer. Damage mechanisms are a complex issue [76]. Among other aspects, the confinement of the area covered with the gold results in a reduced heat dissipation from the illuminated region. This effect is worsened by the low thermal conductivity of the glass substrate. Our test pulse energy was increased gradually as long as an exposure time of 15 min leaves the sample edges unharmed. The maximum intensity applied to the metamaterials was then arbitrarily fixed at one-eighth of the damage threshold which corresponds to a value of 2.3 mJ cm^{-2}.

The measurement may be carried out at cryogenic temperatures. The advantage is twofold. First, the resistivity of the metal drops drastically with temperature and, with it, the

effect of the heating process. Second, the remaining heat is promptly evacuated by the helium gas. We have not tested this method for gold on glass structures yet, as we concentrated on the application of metamaterials on $R\mathrm{MnO_3}$. However, the gold wires on $R\mathrm{MnO_3}$ crystals were cooled below 100 K. No damage by the laser irradiation or the different thermal contraction coefficients of the $R\mathrm{MnO_3}$ and the gold was observed at this temperature.

Furthermore, one could think of exchanging either the metal or the substrate to improve the heat transport. Here, silver and sapphire are ideal candidates. However, silver oxidizes very quickly under ambient conditions which increases the losses. As for sapphire, its high refractive index leads to a pronounced red shift of the linear resonances. This red shift cannot be compensated by further reducing the lateral size of the nanoscopic building blocks due to technological limitations. The red shift also occurs when one embeds the gold structures into a supporting transparent over-layer such as an extra PMMA polymer layer applied to the sample.

Finally, based on the Babinet principle [77, 78], one could maximize the metal volume by writing inverted structures. However, by doing so one deviates from the SRR structures studied in most other works.

5 Experiment: results

5.1 Characterization: SHG spectroscopy

In this section the process of SHG on metamaterials will be characterized by polarization-dependent SHG spectroscopy measurements on the SRR structures shown in Fig. 2. First, we investigate to which extent the spectral dependence of the SHG signal is related to the nonlinear susceptibility $\chi^{(2)}$ and to which extent it is due to linear modifications of the incident light at ω and the emitted light at 2ω. In Fig. 5, we compare the spectral dependence of the SHG signal from χ_{zyy} for a SRR with an y-polarized fundamental resonance at 1.25 eV with its linear extinction spectra. The scale of the linear spectrum is chosen such that any correlation with the SHG signal may be seen more easily at the fundamental frequency or at the SHG frequency. Also, we compare the SHG signal to the χ_{zyy} component spectrum of the first design in Fig. 6, see Sect. 3.1(ii). A lack of correspondence is obvious in this sample as well as in samples with other resonance energies (not shown). We conclude that SHG in metamaterials does not originate from a simple projection of their linear response onto the spectral dependence of the SHG signal. Similarly, one can compare the SHG spectrum to the spectral dependence of the surface-induced SHG signal obtained on the closed gold film in Sect. 4.3, see Fig. 7. For this purpose, the film had to be tilted by 45° because

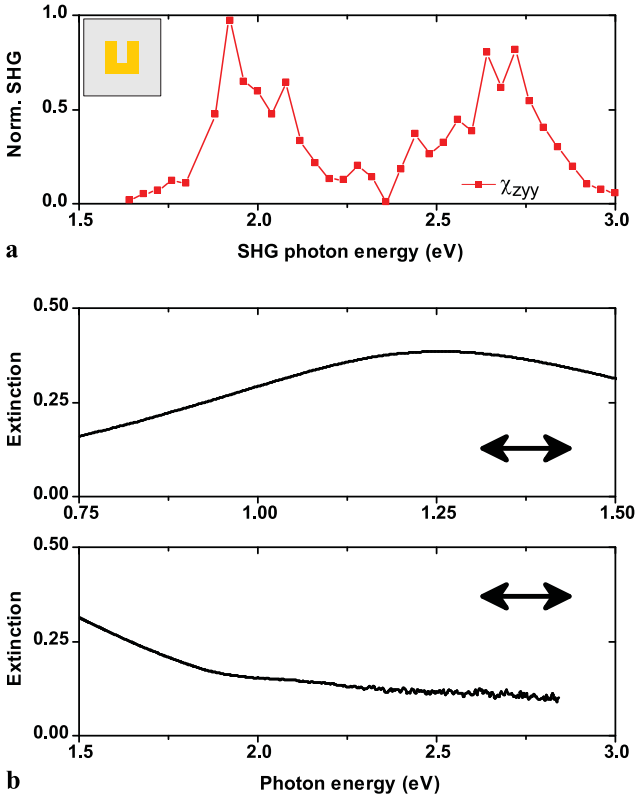

Fig. 5 (**a**) Spectral dependence of the SHG signal from χ_{zyy} and (**b**) the linear extinction spectrum at the frequency of the incident light at ω and of the emitted light at 2ω. The incident light polarization orientation is indicated as inset. The comparison reveals that the SHG spectra reveal a truly nonlinear response of the metamaterials and not merely a projection of linear extinction effects onto the SHG spectrum. Note that the resonance at 1.25 eV corresponds to a fundamental plasmonic resonance

no SHG is expected (and observed) at normal incidence according to [59]. Again, no correlation is observed so that we conclude that the measured SHG spectrum truly reflects the nonlinear optical properties of the metamaterial.

Figure 6 shows an overview of the relative SHG intensity gained from the variety of designs in Fig. 2. The corresponding linear extinction spectra are shown in Fig. 8: The dichroic structures possess a fundamental linear resonance near 0.70 eV for the y eigenpolarization and a higher energy Mie resonance at about 1.15 eV for the z eigenpolarization. Many striking features are observed in the SHG spectra. While in some cases, like for the χ_{zyy} components of the $mm2$ structures, the SHG spectra appear to be correlated to the corresponding horizontally polarized linear spectra, in other cases, such as the χ_{zzz} components with the vertically polarized linear spectra, such a correlation is absent. Thus, it is not possible to confirm a systematic correlation between the spectra at ω and 2ω. In addition, the spectra do not display a narrowing of their FWHM with respect to that of the linear spectra, as one would expect through the SHG process. Therefore, we cannot conclude if linear plas-

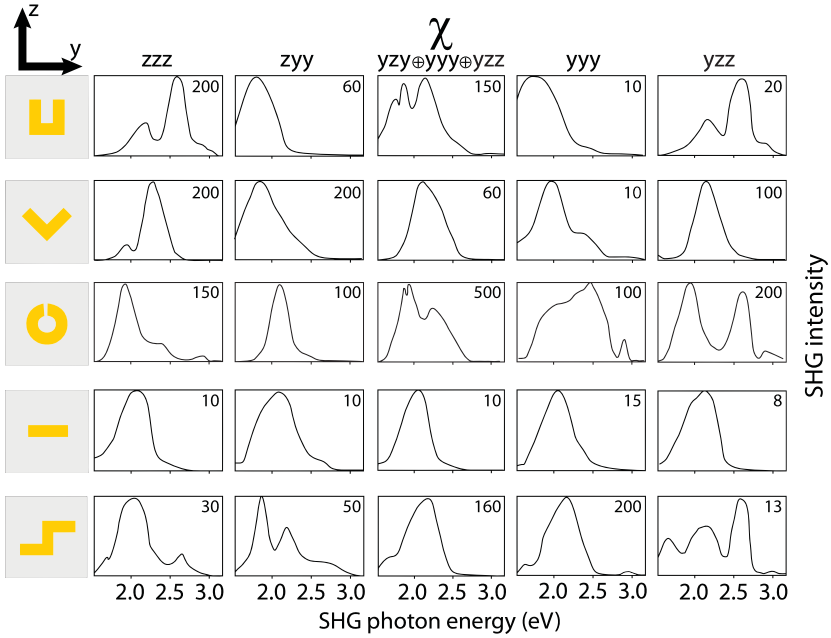

Fig. 6 SHG spectra for metamaterials featuring a variety of designs. The values given as insets represent the peak value of each spectrum on an arbitrary scale. The spectra in the center column represent a convolution of contributions from three independent SHG tensor components

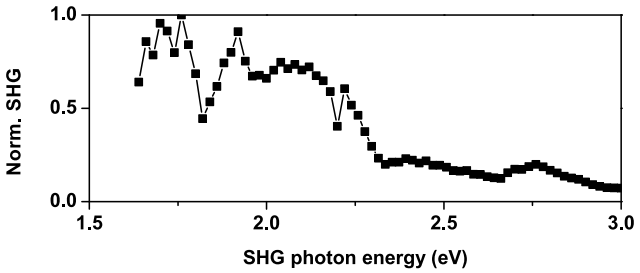

Fig. 7 SHG spectrum of a plain gold film illuminated by p-polarized light at an angle of incidence of 45°

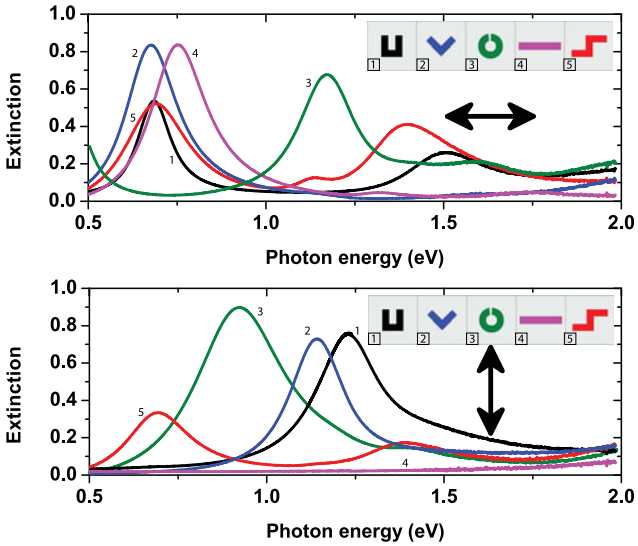

Fig. 8 Linear plasmonic resonances for the structures characterized by SHG. All samples present a fundamental linear resonance with a width of 0.20–0.35 eV, centered around 0.70 eV as well as a higher resonance at about 1.15 eV. The polarization of the incident light is indicated by the arrows. The output polarization is not analyzed

monic resonance or a more subtle process is responsible for the spectral dependence of the SHG signal.

Interestingly, we observe that both y- and z-polarized excitations can lead to SHG signals of equal order of amplitude. Then, on the one hand, the magnetic metamaterial aspect in [44] may not be a suitable interpretation, as the same authors later suggested in [51]. On the other hand, this is consistent with the plasmonic excitation description in [27]. Thus, it is sufficient to define metamaterials according to a metal nanostructure nomenclature.

We now investigate the role of structural complexity by comparison of the SHG spectra of the top three SRR structures in Fig. 6, see Sect. 3.1(iii). Although they share the same $mm2$ geometry, the spectra of corresponding SHG susceptibilities exhibit pronounced differences. However, understanding the underlying processes is not trivial. Our idea was to investigate the role of surface curvature and find possible evidence for local field enhancement at corners, see Sect. 3.1. Indeed, the peak signal between the ⊔-, L-, and C-shaped structures varies, but a systematic relation to the number of corners in the SRR design is not obvious. In several of the spectra (χ_{zzz}, χ_{yyy}, χ_{yzz}) we observe double peaks whose relative amplitude changes with the design. In addition, the change of design is accompanied by red shifts (χ_{zyy}, χ_{yyy}) and blue shifts (χ_{zzz}) of the spectra. The reasons for all these features are not yet understood.

Interestingly, the strongest signal is measured for the round SRRs in the χ_{yzy} configuration. With a peak value of 500, it is more than twice as large as any other signal. For the C-shaped SRR the energy difference between the

two resonances at 0.90 eV and 1.15 eV is the smallest of the SRRs shown here. Therefore, the high SHG intensity may be the result of a constructive interference of the SHG contributions from the two resonances.

We now focus on the two centrosymmetric structures shown at the bottom of Fig. 6 to verify the presence of any SHG contributions that are not due to the leading-order ED type, see Sect. 3.1(iv). The SHG signal observed on the cut-wire structures is approximately zero. For this structure, the point symmetry analysis and the ED approach are therefore the appropriate way to describe the structure. However, the centrosymmetric Z-shaped nanostructures exhibit a SHG signal with an intensity comparable to that measured on the non-centrosymmetric structures. This is corroborated by the observations of other symmetry-forbidden SHG contributions (i.e. χ_{yyy}, χ_{yzz}) even on the non-centrosymmetric designs.

These striking observations show that the description of the metamaterials by an effective SHG susceptibility describing only the global symmetry of the periodic arrangement of nanoscopic building blocks is insufficient. Obviously, the local structure of the building blocks on the nanoscale may lead to contributions to the SHG yield that go beyond those allowed by the macroscopic symmetry. This is similar to the case of incommensurate structures where long-wavelength spin structures were recently found to lead to SHG contributions that are forbidden by the global symmetry [79].

As for the origin of the local SHG contributions we note that, whereas the metamaterials present an excellent homogeneity at the scale of hundreds of nanometers, this is no longer true on the order of the size of the building blocks. A multitude of surface defects with small curvature are present [80, 81]. In spite of their random distribution, they can interfere with the SHG process so that new SHG signals emerge that are normally canceled out due to destructive interference. Also, "hot spots" with high charge density are associated with regions with small radius of curvature. By Gauss's law, the electric field intensity is locally increased and multipoles of even higher order can be promoted.

A qualitative and quantitative evaluation of this interpretation is presently under development. An elaborate approach is found in the recent work of Kauranen et al. [82–84]. Their work make use of an effective medium multipolar tensor analysis to demonstrate the presence of higher-order contributions to the SHG signal due to local effects. The resulting inhomogeneity of the electric field may also lead to SHG contributions from the substrate [82, 85–87]. The relevance of local inhomogeneities for the SHG process is supported by linear extinction spectra and SEM measurements on the metamaterials subsequent to the SHG experiments. We observe that laser-induced modifications increasing the disorder of the building blocks do always occur up to partial detachment and relocation on the substrate as shown in Fig. 4.

5.2 Application: SHG enhancement

In this section, the application potential of metamaterials for enhanced nonlinear optical performance were considered. Metamaterials in the form of wires are written on multiferroic $R\mathrm{MnO_3}$ single crystals and are considered as a "catalyst" for enhancing the SHG conversion efficiencies of the $R\mathrm{MnO_3}$. As explained in Sect. 3.3, patterning the $R\mathrm{MnO_3}$ on the nanoscale is expected to tailor the field distribution within the $R\mathrm{MnO_3}$ crystals so that local peaks of the electric field ensue and enhance the efficiency of the SHG process.

The feasibility of this approach was verified in two steps.

(i) First, we characterized the spectral dependence of the amplification. For this purpose the FEL SHG signal was employed. It is generated in the entire spectral range accessible with our laser system and measurement was done under ambient conditions. In particular, the effect of tuning the resonance of the wires was investigated. As mentioned in Sect. 4.2, the laser light was incident at 45° to the surface of the sample.

(ii) Second, it is important to show that aside from any field enhancement the metamaterials do not affect the basic properties of the host material. This is best verified by investigating the AFM SHG signal and the AFM domain structures of the $R\mathrm{MnO_3}$. The AFM domains are easily moved so that any perturbation by the gold wires applied on the sample are expected to influence or pin the position of AFM domain walls. This experiment has to be done at low temperature and in the narrow spectral range of 2.3–2.8 eV in which an AFM SHG signal is present. Because of these restrictions this will be carried out after some basic understanding of the SHG enhancement has been gained by studying the FEL SHG signal in the first step. As mentioned in Sect. 4.2, the laser light was incident perpendicular to the surface of the sample.

Our first sample was an $\mathrm{YbMnO_3}$ single crystal grown by the floating-zone technique. The reflection spectra are shown in Fig. 9. As explained in Sect. 2.3, the resonance of the nanowires was observed with light polarized perpendicularly to the direction of the wires. Figure 9 shows SHG anisotropy measurements of the unstructured crystal and of the field F2 (vertical wires). For the anisotropy measurement the SHG contribution polarized parallel to the polarization of the incident light was measured while rotating the latter from 0° to 360°. The measurement was carried out at off-resonance conditions: SHG data were taken at 2.80 eV, whereas the resonance of the wires was located at 1.64 eV. We observe two symmetric in-plane lobes in the

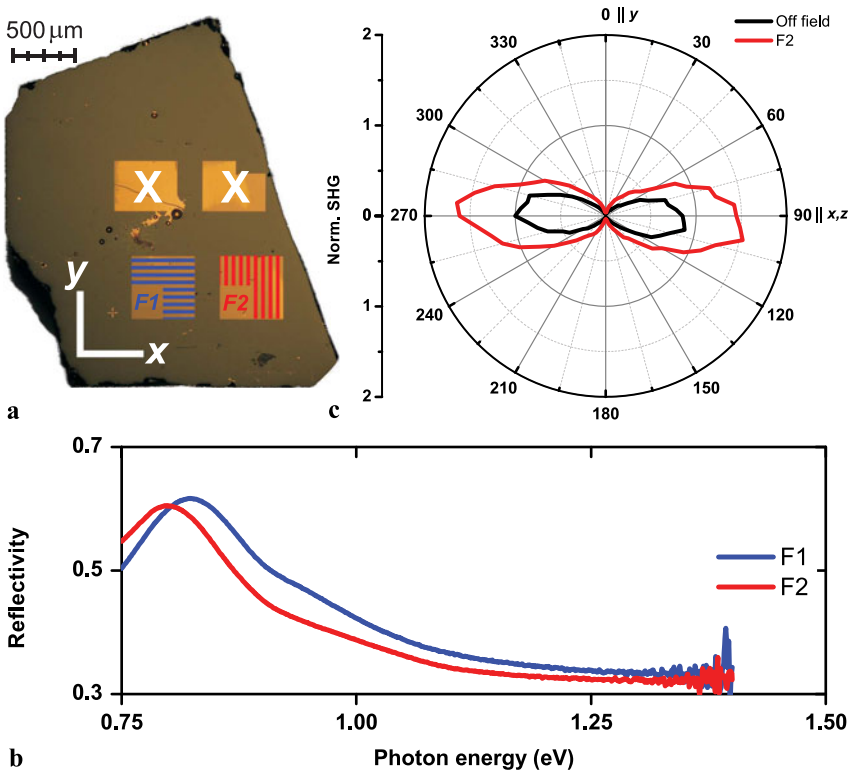

Fig. 9 (**a**) Image of a $YbMnO_3$ single crystal after applying arrangements of gold wires to its polished surface. Arrays damaged by improper lift-off are indicated by an "X" and are not further considered in the experiments. The orientation of the wires is indicated for each field. (**b**) Linear reflectivity for light polarized perpendicular to the wires for the fields F1 and F2. A plasmonic resonance is observed at 0.82 eV. (**c**) SHG anisotropy measurement on the polished $YbMnO_3$ surface and on the field F2 at 2.80 eV. An angle of 0° or 90° corresponds to light polarized along the y-axis or x-axis of the $YbMnO_3$ crystal, respectively. SHG intensities are normalized to the maximum value obtained on the bare crystal

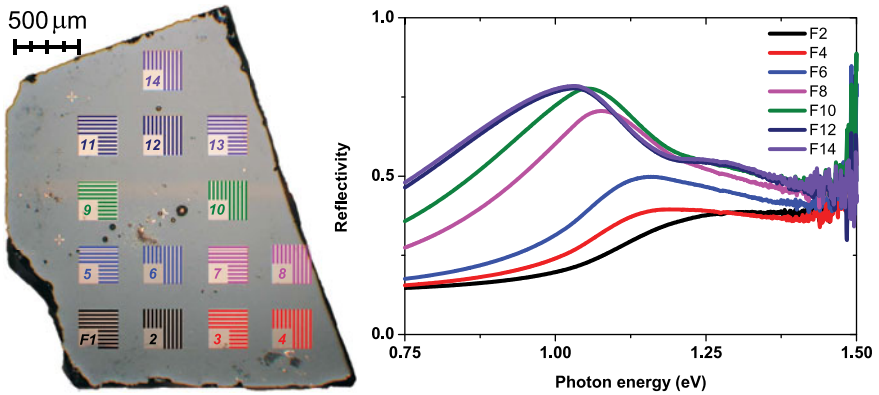

Fig. 10 Image of the $YbMnO_3$ crystal after fabricating a new set of wires, and corresponding linear reflectivity spectra with light polarized perpendicular to the direction of the wires. Only the spectra of the fields with vertical wires are shown. The corresponding spectra for the fields with horizontal wires reveals a reproducibility at least as good as that shown in Fig. 9

SHG anisotropy in accordance with the SHG tensor components in Table 2. In spite of the off-resonance excitation, an enhancement of the SHG signal by a factor two is already observed. When the photon energy of the SHG process is tuned toward the resonance of the gold wires, the SHG signal on the F2 area is further enhanced. However, an absolute value of the amplification is not obtained because of drastic and unsystematic variations of the enhancement among the many different $R MnO_3$ samples investigated in this work. Even the same sample shows different degrees of SHG enhancement after the gold wires are re-fabricated. Some samples show no amplification at all despite their linear resonance being within the FEL signal spectral range, see Fig. 10. Up to present, the reasons for the limited reproducibility are not understood. However, after realizing the importance of inhomogeneities in the local structure of the metamaterials on the scale of the individual building blocks, we suspect that these inhomogeneities may also have a crucial impact on the degree of SHG enhancement observed on the $R MnO_3$ samples. This is supported by the subsequent investigation of the AFM SHG signal on the wire structures investigated by FEL SHG. None of the samples show an amplification of the AFM SHG signal, neither at the resonance of the gold wires nor away from it.

To summarize the experiments on the $R MnO_3$ system, we observed a reproducible enhancement of the FEL SHG signal on a variety of samples with a well-understood polarization dependence. However, the variation of the effect

between samples is immense and not controlled yet. An enhancement of the AFM SHG signal was not observed so far. The local nanoscopic homogeneity and stability of the metamaterials providing the enhancement seems to be a key for this behavior.

6 Conclusion

Polarization-dependent nonlinear optical spectroscopy in the form of SHG was applied to different types of metamaterial: Two-dimensional periodic arrays of gold nanostructures on a glass substrate and periodically spaced arrangements of gold wires on multiferroic $R\mathrm{MnO_3}$ single crystals. Investigations of the former system were targeted at a basic characterization of the nonlinear optical response spectrum of metamaterials. Investigations of the latter system were aimed at probing the feasibility of metamaterials for enhancing the nonlinear optical performance of functional compounds.

We found that the SHG spectra do not show a systematic dependence on the shape, size, and symmetry of the nanoscopic building blocks constituting the metamaterial so that their interpretation remains ambiguous. However, we showed that similar SHG signal strengths for y- and z-polarized excitations support the plasmonic description for the resonances of the linear spectra. We described how additional SHG contributions that are forbidden by the global point group symmetry of the ideal periodic structures can emerge due to local effects. Concerning functionality, a pronounced enhancement of the SHG yield of multiferroic $R\mathrm{MnO_3}$ single crystals due to the local field enhancement exerted by the metamaterials was observed, yet with a substantial and still uncontrolled sample dependence of the enhancement.

Both experiments reveal that a comprehensive understanding of the nonlinear optical properties of metamaterials requires one to go beyond a structural and symmetry analysis on the macroscopic level. Instead, local aspects of the design of the metamaterial on the level of the building blocks has to be taken into account. The homogeneity and the degree of periodicity of the metamaterials on this nanoscopic level seems to have a major impact on the quality and reproducibility of the nonlinear optical response and poses a great challenge for future investigations.

Acknowledgement The authors acknowledge support by the DFG Research Unit 557.

References

1. V.G. Veselago, Sov. Phys. Usp. **10**, 509 (1968)
2. J. Pendry, A. Holden, D.J. Robbins, W.J. Stewart, Microw. Theory **47**, 2075 (1999)
3. D.R. Smith, W.J. Padilla, J. Willie, D.C. Vier, S.C. Nemat-Nasser, S. Schultz, Phys. Rev. Lett. **84**, 4184 (2000)
4. D.R. Smith, J.B. Pendry, M.C.K. Wiltshire, Science **305**, 788 (2004)
5. C.M. Soukoulis, S. Linden, M. Wegener, Science **315**, 47 (2007)
6. C. Soukoulis, M. Kafesaki, E. Economou, Adv. Mater. **18**, 1941 (2006)
7. V.M. Shalaev, Nat. Photonics **1**, 41 (2007)
8. S. Linden, M. Wegener, Phys. J. **5**, 29 (2006)
9. U. Kreibig, P. Zacharias, Z. Phys. A **231**, 128 (1970)
10. M.C. Daniel, D. Astruc, Chem. Rev. **104**, 293 (2004)
11. V.A. Podolskiy, A.K. Sarychev, V.M. Shalaev, Opt. Express **11**, 735 (2003)
12. V.A. Podolskiy, A.K. Sarychev, E.E. Narimanov, V.M. Shalaev, J. Opt. A **7**, S32 (2005)
13. S. Linden, C. Enkrich, M. Wegener, J. Zhou, Th. Koschny, C.M. Soukoulis, Science **306**, 1351 (2004)
14. S. Zhang, W. Fan, K.J. Malloy, S.R. Brueck, N.C. Panoiu, R.M. Osgood, Opt. Express **13**, 4922 (2005)
15. G. Dolling, C. Enkrich, M. Wegener, C.M. Soukoulis, S. Linden, Science **312**, 892 (2006)
16. M.S. Rill, C. Plet, M. Thiel, I. Staude, G. von Freymann, S. Linden, M. Wegener, Nat. Mater. **7**, 543 (2008)
17. H. Schweizer, L. Fu, H. Gräbeldinger, H. Guo, N. Liu, S. Kaiser, H. Giessen, Phys. Status Solidi A **204**, 3886 (2007)
18. G. Dolling, C. Enkrich, M. Wegener, J.F. Zhou, C.M. Soukoulis, S. Linden, Opt. Express **30**, 3198 (2005)
19. J.B. Pendry, A.J. Holden, W.J. Stewart, I. Youngs, Phys. Rev. Lett. **76**, 4773 (1996)
20. J.B. Pendry, Phys. Rev. Lett. **85**, 3966 (2000)
21. N. Fang, H. Lee, C. Sun, X. Zhang, Science **308**, 534 (2005)
22. Z. Liu, H. Lee, Y. Xiong, C. Sun, X. Zhang, Science **315**, 1686 (2007)
23. J.B. Pendry, D. Schurig, D.R. Smith, Science **312**, 1780 (2006)
24. D. Schurig, J.J. Mock, B.J. Justice, S.A. Cummer, J.B. Pendry, A.F. Starr, D.R. Smith, Science **314**, 977 (2006)
25. J.K. Rowling, Harry Potter and the Philosopher's Stone (Bloomsbury, 1997)
26. J. Valentine, J. Li, T. Zentgraf, G. Bartal, X. Zhang, Nat. Mater. **8**, 568 (2009)
27. C. Rockstuhl, F. Lederer, C. Etrich, T. Zentgraf, J. Kuhl, H. Giessen, Opt. Express **14**, 8827 (2006)
28. R.A. Shelby, D.R. Smith, S. Schultz, Science **292**, 77 (2001)
29. T.J. Yen, W.J. Padilla, N. Fang, D.C. Vier, D.R. Smith, J.B. Pendry, D.N. Basov, X. Zhang, Science **303**, 1494 (2004)
30. C. Enkrich, M. Wegener, S. Linden, S. Burger, L. Zschiedrich, F. Schmidt, J.F. Zhou, T. Koschny, C.M. Soukoulis, Phys. Rev. Lett. **95**, 203901 (2005)
31. A.N. Grigorenko, A.K. Geim, H.F. Gleeson, Y. Zhang, A.A. Firsov, I.Y. Khrushchev, J. Petrovic, Nature **438**, 335 (2005)
32. M.W. Klein, C. Enkrich, M. Wegener, C.M. Soukoulis, S. Linden, Opt. Lett. **31**, 1259 (2006)
33. W.J. Padilla, A.J. Taylor, C. Highstrete, M. Lee, R.D. Averitt, Phys. Rev. Lett. **96**, 107401 (2006)
34. D.R. Smith, S. Schultz, P. Markoš, C.M. Soukoulis, Phys. Rev. B **65**, 195104 (2002)
35. S. O'Brien, D. McPeake, S.A. Ramakrishna, J.B. Pendry, Phys. Rev. B **69**, 241101 (2004)
36. J. Zhou, T. Koschny, M. Kafesaki, E.N. Economou, J.B. Pendry, C.M. Soukoulis, Phys. Rev. Lett. **95**, 223902 (2005)
37. K. Chen, C. Durak, J.R. Heflin, H.D. Robinson, Nano Lett. **7**, 254 (2007)
38. F.B.P. Niesler, N. Feth, S. Linden, J. Niegemann, J. Gieseler, K. Busch, M. Wegener, Opt. Lett. **34**, 1997 (2009)
39. P.A. Franken, A.E. Hill, C.W. Peters, G. Weinreich, Phys. Rev. Lett. **7**, 118 (1961)

40. N. Bloembergen, *Nonlinear Optics* (World Scientific, Singapore, 1996)
41. Y.R. Shen, *The Principles of Nonlinear Optics* (Wiley-Interscience, New York, 2002)
42. R.W. Boyd, *Nonlinear Optics* (Academic Press, New York, 2008)
43. K.H. Bennemann, *Nonlinear Optics in Metals* (Oxford University Press, Oxford, 1999)
44. M.W. Klein, C. Enkrich, M. Wegener, S. Linden, Science **313**, 502 (2006)
45. M.W. Klein, M. Wegener, N. Feth, S. Linden, Opt. Express **15**, 5238 (2007)
46. R. Singh, C. Rockstuhl, F. Lederer, W. Zhang, Appl. Phys. Lett. **94**, 021116 (2009)
47. N. Liu, H. Giessen, Angew. Chem., Int. Ed. **49**, 9838 (2010)
48. H.J. Simon, D.E. Mitchell, J.G. Watson, Phys. Rev. Lett. **33**, 1531 (1974)
49. A. Lesuffleur, L.K.S. Kumar, R. Gordon, Appl. Phys. Lett. **88**, 261104 (2006)
50. J.A.H. Nieuwstadtvan, M. Sandtke, R.H. Harmsen, F.B. Segerink, J.C. Prangsma, S. Enoch, L. Kuipers, Phys. Rev. Lett. **97**, 146102 (2006)
51. N. Feth, S. Linden, M.W. Klein, M. Decker, F.B.P. Niesler, Y. Zeng, W. Hoyer, J. Liu, S.W. Koch, J.V. Moloney, M. Wegener, Opt. Lett. **33**, 1975 (2008)
52. E. Kim, F. Wang, W. Wu, Z. Yu, Y.R. Shen, Phys. Rev. B **78**, 113102 (2008)
53. Y. Zeng, W. Hoyer, J. Liu, S.W. Koch, J.V. Moloney, Phys. Rev. B **79**, 235109 (2009)
54. F.B.P. Niesler, N. Feth, S. Linden, M. Wegener, Opt. Lett. **36**, 1533 (2011)
55. T.H. Maiman, Nature **187**, 493 (1960)
56. P.S. Pershan, Phys. Rev. **130**, 919 (1963)
57. N. Bloembergen, R.K. Chang, S.S. Jha, C.H. Lee, Phys. Rev. **174**, 813 (1968)
58. P. Guyot-Sionnest, Y.R. Shen, Phys. Rev. B **38**, 7985 (1988)
59. R.R. Birss, *Symmetry and Magnetism* (Elsevier, Amsterdam, 1966)
60. P. Guyot-Sionnest, W. Chen, Y.R. Shen, Phys. Rev. B **33**, 8254 (1986)
61. P. Drude, Ann. Phys. **306**, 566 (1900)
62. P.B. Johnson, R.W. Christy, Phys. Rev. B **6**, 4370 (1972)
63. G. Mie, Ann. Phys. **330**, 377 (1908)
64. A. Taflove, S.C. Hagness, *Computational Electrodynamics: The Finite-Difference Time-Domain Method* (Artech House, Norwood, 2005)
65. B. Lamprecht, J. Krenn, A. Leitner, F. Aussenegg, Appl. Phys. B **69**, 223 (1999)
66. C. Sönnichsen, T. Franzl, T. Wilk, G. von Plessen, J. Feldmann, O. Wilson, P. Mulvaney, Phys. Rev. Lett. **88**, 077402 (2002)
67. U. Kreibig, M. Vollmer, *Optical Properties of Metal Clusters* (Springer, Berlin, 1995)
68. B. Lamprecht, A. Leitner, F. Aussenegg, Appl. Phys. B **68**, 419 (1999)
69. H. Tuovinen, M. Kauranen, K. Jefimovs, P. Vahimaa, T. Vallius, J. Turunen, N.V. Tkachenko, H. Lemmetyinen, J. Nonlinear Opt. Phys. Mater. **11**, 421 (2002)
70. B. Canfield, S. Kujala, K. Jefimovs, J. Turunen, M. Kauranen, Opt. Express **12**, 5418 (2004)
71. B.K. Canfield, S. Kujala, K. Jefimovs, T. Vallius, J. Turunen, M. Kauranen, J. Opt. A **7**, S110 (2005)
72. M. Fiebig, J. Phys. D, Appl. Phys. **38**, R123 (2005)
73. M. Fiebig, D. Fröhlich, K. Kohn, S. Leute, T. Lottermoser, V.V. Pavlov, R.V. Pisarev, Phys. Rev. Lett. **84**, 5620 (2000)
74. M. Fiebig, T. Lottermoser, R.V. Pisarev, J. Appl. Phys. **93**, 8194 (2003)
75. D. Sa, R. Valentí, C. Gros, Eur. Phys. J. B **14**, 301 (2000)
76. A. Habenicht, PhD thesis, 2007
77. F. Falcone, T. Lopetegi, M.A.G. Laso, J.D. Baena, J. Bonache, M. Beruete, R. Marqués, F. Martin, M. Sorolla, Phys. Rev. Lett. **93**, 197401 (2004)
78. T. Zentgraf, T.P. Meyrath, A. Seidel, S. Kaiser, H. Giessen, C. Rockstuhl, F. Lederer, Phys. Rev. B **76**, 033407 (2007)
79. D. Meier, N. Leo, G. Yuan, T. Lottermoser, M. Fiebig, P. Becker, L. Bohatý, Phys. Rev. B **82**, 155112 (2010)
80. B.K. Canfield, H. Husu, J. Laukkanen, B. Bai, M. Kuittinen, J. Turunen, M. Kauranen, Nano Lett. **7**, 1251 (2007)
81. M. Lippitz, M.A. Dijkvan, M. Orrit, Nano Lett. **5**, 799 (2005)
82. B.K. Canfield, S. Kujala, K. Jefimovs, Y. Svirko, J. Turunen, M. Kauranen, J. Opt. A **8**, S278 (2006)
83. M. Kauranen, S. Cattaneo, Prog. Opt. **51**, 69 (2008)
84. M. Zdanowicz, S. Kujala, H. Husu, M. Kauranen, New J. Phys. **13**, 023025 (2011)
85. S. Cattaneo, M. Kauranen, Phys. Rev. B **72**, 033412 (2005)
86. F.J. Rodriguez, F.X. Wang, B.K. Canfield, S. Cattaneo, M. Kauranen, Opt. Express **15**, 8695 (2007)
87. F.J. Rodriguez, F.X. Wang, M. Kauranen, Opt. Express **16**, 8704 (2008)